Molecular Basis for Cation Selectivity in Claudin-2–based Paracellular Pores: Identification of an Electrostatic Interaction Site

Alan S.L. Yu,[1,2] Mary H. Cheng,[3] Susanne Angelow,[1] Dorothee Günzel,[4] Sanae A. Kanzawa,[1] Eveline E. Schneeberger,[5] Michael Fromm,[4] and Rob D. Coalson[3]

[1]Division of Nephrology, Department of Medicine, and [2]Department of Physiology and Biophysics, University of Southern California Keck School of Medicine, Los Angeles, CA 90089
[3]Department of Chemistry, University of Pittsburgh, Pittsburgh, PA 15260
[4]Institute of Clinical Physiology, Charité, Campus Benjamin Franklin, 12200 Berlin, Germany
[5]Department of Pathology, Massachusetts General Hospital, Boston, MA 02114

Paracellular ion transport in epithelia is mediated by pores formed by members of the claudin family. The degree of selectivity and the molecular mechanism of ion permeation through claudin pores are poorly understood. By expressing a high-conductance claudin isoform, claudin-2, in high-resistance Madin-Darby canine kidney cells under the control of an inducible promoter, we were able to quantitate claudin pore permeability. Claudin-2 pores were found to be narrow, fluid filled, and cation selective. Charge selectivity was mediated by the electrostatic interaction of partially dehydrated permeating cations with a negatively charged site within the pore that is formed by the side chain carboxyl group of aspartate-65. Thus, paracellular pores use intrapore electrostatic binding sites to achieve a high conductance with a high degree of charge selectivity.

The Journal of General Physiology

INTRODUCTION

Epithelia transport solutes and water between body compartments and external surfaces, using both transcellular and paracellular routes. Paracellular ion transport is believed to occur through pores in the tight junction (for review see Reuss, 2001). These pores are now known to be formed by four–transmembrane domain proteins known as claudins (Tsukita and Furuse, 2000; Van Itallie and Anderson, 2006). In channels that mediate transcellular transport, ions move perpendicular to the plane of the cell membrane, traversing the low-dielectric environment at the interior of the lipid bilayer, with stabilization and selectivity conferred by the transmembrane domains of the pore protein. Paracellular ion permeation through claudins is likely to be quite different because ions move parallel to and extracellular to the plane of the lipid bilayer (Fig. 1). This pathway is potentially highly hydrated and lined predominantly by the extracellular domains of claudins. The permeability properties of the native paracellular pathway have been carefully characterized in leaky epithelia, such as rabbit gallbladder (Barry et al., 1971; Wright et al., 1971) and cultured kidney tubule cell lines (Cereijido et al., 1978). However, the degree to which claudin-based pores exhibit ion selectivity and the underlying molecular mechanisms are poorly understood.

Attempts to measure claudin permeability quantitatively in an overexpression system have been hampered by the fact that many claudins behave predominantly as barriers rather than pores. Those that do increase permeability mostly increase it modestly above background, and such results are confounded by the contribution of background permeability due to endogenous claudins that are present in all epithelial cells (Furuse et al., 2001; Van Itallie et al., 2001, 2003, 2006; Amasheh et al., 2002; Yu et al., 2003; Alexandre et al., 2005; Hou et al., 2005; Angelow et al., 2007a). To solve this, we exploited the observation that claudin-2, when expressed in high-resistance strains of Madin-Darby canine kidney (MDCK) cells, exhibits a large increase in conductance and a high signal to noise ratio (Furuse et al., 2001; Amasheh et al., 2002). We developed an inducible cell line based on this, so that background permeability due to endogenous host cell claudins could be determined in the uninduced state and subtracted from the permeability in the induced state, yielding a quantitative measure of claudin-2 permeability.

MATERIALS AND METHODS

Generation and Characterization of MDCK I TetOff Claudin-2 Stable Cell Lines

Retroviral transduction was performed as described previously (Yu et al., 2003). cDNA encoding the coding region of wild-type

Correspondence to Alan S.L. Yu: alanyu@usc.edu

Abbreviations used in this paper: DMC, dynamic Monte Carlo; MDCK, Madin-Darby canine kidney; TM, triple mutant; WT, wild-type.

The Rockefeller University Press $30.00
J. Gen. Physiol. Vol. 133 No. 1 111–127
www.jgp.org/cgi/doi/10.1085/jgp.200810154

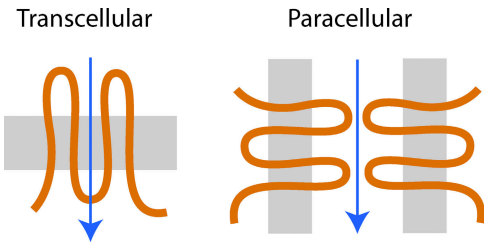

Figure 1. Comparison of the different transepithelial transport routes. Transcellular/transmembrane channels (left) mediate ion transport (arrow) perpendicular to the plane of the lipid bilayer (gray), with the pore wall formed predominantly by intramembrane domains of the channel polypeptide (orange). Paracellular pores such as claudins (right) mediate transport parallel to and extracellular to the lipid bilayer, with the pore walls presumably constituted by the extracellular domains of claudin polypeptides.

(WT) mouse claudin-2 or mutants generated by site-directed mutagenesis (QuikChange kit; Agilent Technologies) were cloned downstream of the Tet-responsive element into pRevTREP, lipofected into the viral packaging line, PT67, and a stable polyclonal population selected with hygromycin. Viral supernatant was then used to infect MDCK I TetOff cells (Angelow et al., 2007b) in the presence of polybrene, and stable clones were selected using cloning cylinders. High-throughput screening of clones was performed by seeding them into optical glass-bottomed 96-well culture plates (Thermo Fisher Scientific) in the presence (Dox+) or absence (Dox−) of 20 ng/ml doxycycline, immunostaining them with claudin-2 antibody (Invitrogen), and identifying positive clones by fluorescence microscopy. Double labeling with anti-ZO1 (Invitrogen) was used to confirm correct localization of claudin-2 to the tight junction. Claudin-2 protein expression was confirmed by immunoblotting. An infrared fluorescence secondary antibody (Alexa Fluor 680) was used so that blots could be scanned with an infrared detection system (Li-Cor Odyssey) and the bands digitally quantitated. The effect of claudin-2 on expression of endogenous tight junction proteins was assessed by immunoblotting with antibodies to claudins 1, 3, 4, and 7 (Invitrogen).

For freeze-fracture electron microscopy, confluent monolayers were fixed in 2% glutaraldehyde at 4°C for 30 min and processed as described previously (Yu et al., 2003). To quantify the number of parallel strands in the tight junctions, electron micrographs were overlayed with a transparency marked with gridlines, and the number of strands crossing each line was counted. The difference in the median number of strands between Dox+ and Dox− cells was compared using the Wilcoxon ranked-sum test.

Ussing Chamber Electrophysiological Studies

Our methods are identical to those described previously (Yu et al., 2003; Angelow et al., 2006), with the exception that we have modified the way we correct for liquid junction potentials (vide infra). Cells were plated at confluent density on Snapwell filters (Corning) and cultured for 8 d, which we find is sufficient to achieve steady-state transepithelial resistance and maximal induction of expression in the TetOff system. The filters were mounted in Ussing chambers stirred with gas lifts in 100% O_2 at 37°C, and voltage/current clamped using Ag/AgCl electrodes bridged by 3 M KCl/3% agar pipettes. The standard Ringer solution used at baseline contained (in mM): 150 NaCl, 2 $CaCl_2$, 1 $MgCl_2$, 10 glucose, and 10 Tris-HEPES, pH 7.4. In general, data were acquired at 1-s intervals using Acquire and Analyze software (Physiological Instruments). Conductance and voltage measurements for each condition were derived by averaging 5–10 s worth of data (depending on stability) and reported as a single measurement for each monolayer.

In previous studies, we subtracted from the voltage measurements performed on cell monolayer voltages measured under identical conditions using blank filters, in an attempt to correct for liquid junction potentials at the pipette tips. This is a widely used technique (Van Itallie et al., 2001; Yu et al., 2003; Hou et al., 2008). However, we now realize that this is inaccurate because there is also a liquid junction potential across the filter itself when it is blank, but not when cells are cultured on it. Therefore, to deduce the pipette potentials, we had to correct for this blank filter junction potential. Fig. 2 A shows the Ussing chamber setup with a blank filter. The diffusion potential measured experimentally in this way is V_{EF}, where,

$$V_{EF} = (V_L{}^b - V_L{}^a) + V_F. \quad (1)$$

The blank filter behaves like a liquid junction, so V_F was calculated using the generalized Henderson-Planck equation (Barry and Diamond, 1970). Using this value and Eq. 1, we calculated the difference in pipette potentials, $(V_L{}^b - V_L{}^a)$. Fig. 2 B shows the Ussing chamber setup with a cell monolayer inserted. The true transmonolayer diffusion potential, V_M, was deduced from the experimentally measured potential, V_{EM}, by subtracting the pipette potential:

$$V_M = V_{EM} - (V_L{}^b - V_L{}^a). \quad (2)$$

The complete rationale for this, detailed studies to support the use of this method, and the numerical values used for correction are described in Online Supplemental Material II, which is available at http://www.jgp.org/cgi/content/full/jgp.200810154/DC1.

NaCl dilution potentials were measured by switching one hemichamber (usually basolateral) to solution containing different concentrations of NaCl (typically 75 mM) with the other components identical to the standard Ringer. The osmolality was balanced using mannitol. For alkali metal biionic potentials, one hemichamber was switched to a solution containing 150 mM of the alkali metal cation chloride salt. For organic cation diffusion potentials, we used a solution containing 75 mM of the organic cation chloride salt and 75 mM NaCl. Ion permeability ratios were deduced from the Goldman-Hodgkin-Katz voltage equation. For dilution potentials,

$$V = -\frac{RT}{F}\ln\left[\frac{(\alpha+\beta)}{1+\alpha\beta}\right], \quad (3)$$

where V is the apical voltage with respect to the basolateral side, $\beta = P_{Cl}/P_{Na}$, α is the activity ratio of NaCl in apical compared with basolateral compartments, and the individual ion activity coefficients of Na^+ and Cl^- are assumed to be the same (Guggenheim assumption). This can be rearranged to:

$$\beta = \frac{\alpha - x}{\alpha x - 1}, \quad (4)$$

where $x = e^{-VF/RT}$. The activity coefficients used for NaCl at 150 and 75 mM were 0.752 and 0.797, respectively. The additional Cl^- arising from the presence of $CaCl_2$ and $MgCl_2$ in the solutions was ignored, an approximation that should introduce <2% error. Absolute permeabilities were estimated by the method of Kimizuka and Koketsu (1964), as we have described (Yu et al., 2003; Angelow et al., 2006).

$$P_{Na} = \frac{RT}{F^2}\cdot\frac{G_M}{a(1+\beta)}, \quad (5)$$

where a, the Na^+ activity at 150 mM concentration, is 112.8 mM.

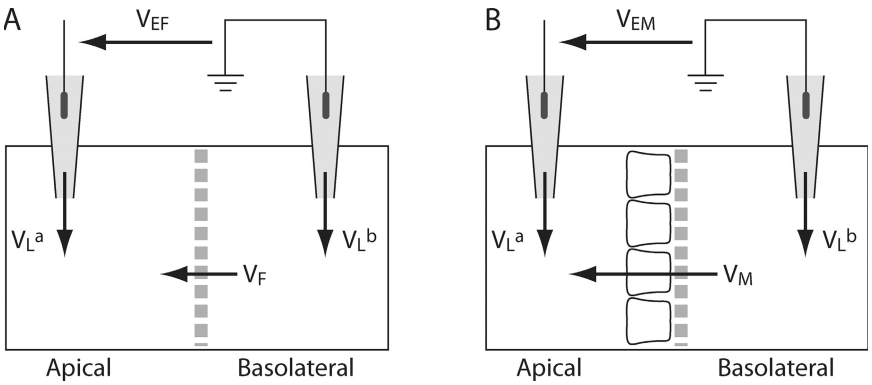

Figure 2. Ussing chamber setup and method of correcting for junction potentials. The sign of the potential is indicated by the arrows, which show the potential of the arrow head with respect to the arrow tail. Liquid junction potentials in the agar bridge pipettes (V_L^a and V_L^b) are calculated as the potential of the solution with respect to the pipette. V_{EF} and V_{EM} are the apparent apical-basolateral potentials that are measured experimentally. (A) Setup with only a blank filter inserted between the hemichambers. The potential across the blank filter, V_F, is defined as the apical potential with respect to the basolateral side. (B) Setup with a filter on which a monolayer of cells has been cultured. The potential across the monolayer and its filter is V_M.

For biionic potentials in which the basolateral chamber was exchanged from 150 mM NaCl to 150 mM M^+Cl^- (where M^+ is another inorganic or organic cation),

$$V = \frac{RT}{F}\ln\left(\frac{\gamma+\beta}{1+\beta}\right), \quad (6)$$

where $\gamma = P_M/P_{Na}$. The mean activity coefficient of each monovalent cation halide salt was assumed to be the same as that of NaCl. The error in determination of the permeability ratio from this approximation was estimated to be no more than 4%.

Claudin-2 pore size was estimated by a Renkin sieving model (Renkin, 1954) in which the pore was assumed to be a cylinder of diameter, *D*, across which spherical cations of diameter, *d*, diffuse. For the sake of simplicity, the sole source of friction was assumed to be hydrodynamic drag, which, according to the Stokes-Einstein relationship, is proportional to *d* (Dwyer et al., 1980). Thus, the apparent permeability of each organic cation, *P*, was fit by nonlinear regression to the equation,

$$P = \frac{A}{d}\left(1-\frac{d}{D}\right)^2, \quad (7)$$

where A is a composite constant reflecting both intrinsic pore properties and the number of pores. Organic cation diameters were derived from empirical data by Hille using Corey-Pauling-Koltum space-filling molecular models (Dwyer et al., 1980).

For studies of acidification, concentrated HCl was added to one or both hemichambers (in most studies to achieve a final pH of 4), and conductance was monitored at 1-s intervals. The rate of change of conductance was fitted to a single exponential curve. The titration curve of conductance, G, at different pH was fit to a Hill equation,

$$G = G_{\max}\left\{\frac{K_a + \alpha\left[H^+\right]^n}{K_a + \left[H^+\right]^n}\right\}, \quad (8)$$

where G_{max} is the maximum conductance, and α is a proportionality constant. Values for the equilibrium constant, K_a, and the Hill coefficient, *n*, were then estimated.

In studies of temperature dependence, the temperature in the Ussing chamber was directly monitored by immersion of a metal thermocouple probe, and the water bath was adjusted to achieve target solution temperatures in the range of 16 to 37°C. Data for each monolayer was then fitted by nonlinear regression to the Arrhenius equation to obtain an individual best-fit estimate of the activation energy (Yu et al., 2003; Angelow et al., 2006).

Conductance Scanning

The relative conductance of trans- and paracellular pathways in the claudin-2–expressing cells was determined by high-resolution conductance scanning of cell monolayers in horizontal Ussing chambers, as described previously (Gitter et al., 1997). An alternating current (24 Hz, 20 μA) was passed across the epithelium, and the electric field generated in the apical bath solution was measured with a pair of microelectrodes (vertical tip distance, 30–80 μm) held above the epithelial surface. With the electric field measured and the specific resistivity of the solution, the local current density was calculated. This and the transepithelial voltage yielded the local conductance, which was measured in the center of the cell body and at the lateral border directly over the tight junction.

Radiotracer Flux Assay

Unidirectional fluxes of $^{45}Ca^{2+}$ were measured in 1-cm^2 Transwell filters, as described previously (Yu et al., 2003). In brief, cells were bathed in DMEM with 5% FBS (Ca^{2+} concentration of 1.8 mM). Trace $^{45}CaCl$ was added to the apical compartment to achieve a specific activity of >50 Ci/mol. At 0.5-, 1-, and 2-h intervals (during which transport was linear), 100 μl of solution was withdrawn from the basolateral compartment for scintillation counting.

Statistical Analysis

Where permeability or conductance of claudin-2 is reported, we took measurements obtained in Dox+ cells and subtracted them from the values in Dox− cells studied in parallel. Values are reported as mean ± SE of measurements performed on three monolayers for each condition, unless otherwise specified, and are representative of at least two independent experiments. Differences between the means of continuously distributed variables were assessed by the two-tailed unpaired *t* test, or one-way ANOVA with Tukey's correction for multiple comparisons, as appropriate. $P < 0.05$ was considered statistically significant.

Brownian Dynamics Simulation

Given the lack of structural detail available for this channel, we built our model of claudin-2 in rough analogy to cation-selective ligand-gated ion channels (e.g., nicotinic acetylcholine receptors), based on the following points of similarity: (1) minimum pore radius; (2) cation selectivity; and (3) channel pore constriction at the location of critical charged groups (Imoto et al., 1988), which helps to confer cation selectivity, inter alia. The rationale for designing our model channel is to qualitatively support the experimental electrophysiology studies reported in this work.

In our Brownian dynamics simulations, claudin-2 was modeled as a cylindrical pore with a diameter of 6.5 Å, based on our experimental estimates (Fig. 7 B). The pore was assumed to have a length of 10 Å, connected to two cone-like vestibules on either side, which represent the entrances to the pore and are in contact with the extracellular solution (Fig. 11 A) (see Online Supplemental Material II for details of our simulations, including the channel geometry; Fig. S4; both are available at http://www.jgp.org/cgi/content/full/jgp.200810154/DC1). The widest part of these vestibules was assumed to be 7.6 Å in radius, and the entire length of the paracellular pore was assumed to be 32 Å. For simplicity, the dielectric constant inside the aqueous pore was assumed to be the same as that in the bulk solution (Graf et al., 2000, 2004; Cheng et al., 2005), with $\varepsilon_w = 80$, and the cell/claudin-2 was characterized by a uniform effective dielectric constant, $\varepsilon_p = 20$, which falls within the range of previously adopted protein dielectric constant (Smith et al., 1993; Simonson and Brooks, 1996; Pitera et al., 2001). For transmembrane ion channels (Corry et al., 2001; Cheng et al., 2005), a comparatively smaller ε_p (i.e., $\varepsilon_p = 2$–5) is usually used to account for the low dielectric constant in the interior of lipids (i.e., $\varepsilon = 2$) (Pethig, 1979). For a paracellular pore, we anticipate a larger effective dielectric constant should be used for ε_p because the pore is formed by the extracellular protein (i.e., $\varepsilon_p = 10$–40) and the dipole layer (Andersen and Fuchs, 1975) formed by the lipid head groups may contribute to an increase in the effective dielectric constant for the cell. D65 was treated explicitly as a negatively charged spherical particle to mimic the carboxylate moiety of this residue, which is characterized by its size R_D, charge q_D, and the distance between the channel centerline and the sphere center R_C, and located in the middle of the pore. The particle description of D65 allowed us to preserve some molecular-level properties of the D65 residue. All other charged residues (E53, D76, R30, and K48) in the first extracellular domain were treated as point charges, and the calculation of electrostatic potential due to these charges was performed by solving Poisson's equation. Claudins are multimeric and have been proposed to form hexamers (Mitic et al., 2003); therefore, residue point charges and D65 particles were inserted six times, 60° apart. The effective charges were assumed to be 0.2 e and −0.2 e for positive and negative point charges, respectively. For simplicity, the positive charges were assumed to face away from the channel and be separated from their neighboring negative charges by 2.5 Å in the radial direction (perpendicular to the channel axis; compare Fig. 11 A).

We used a dynamic Monte Carlo (DMC) method to simulate ion permeation through the claudin-2 paracellular pore. Complete computational details of our DMC algorithm and its application to ion permeation through protein channels can be found in the literature (Graf et al., 2000; Cheng et al., 2005, 2007; Cheng and Coalson, 2005). In our DMC algorithm for ion permeation, configurations were generated by random changes of the ion positions. The total number of ions was characterized by $N = N_L + N_R + N_I + N_v$. Here, N_L and N_R are the fixed numbers of ions on the left and right boundaries (gray buffer regions in Fig. 11 A), which were obtained by integrating the given boundary concentrations C_L and C_R over the volumes of the boundary layers. The constant concentration boundary condition was imposed by randomly distributing N_L or N_R ions in the buffer regions at each Monte Carlo cycle. N_I is the number of ions inside the system, and N_v is the number of virtual ions. The total number of ions N is fixed, and N_I fluctuates. N_v was introduced only for counting purposes and is included to account for dynamic fluctuation of the number of ions in the interior of the system, and to ensure the proportionality of Monte Carlo cycles to real time (Graf et al., 2000).

One Monte Carlo cycle consisted of N steps. At each step, one ion k was randomly chosen to move $\pm h$ in one direction (x, y, or z) if the chosen ion was not a virtual one, where h is a position-dependent displacement for ion k, as detailed below. In the present implementation, this new configuration was accepted if $Rand < \exp(-\beta\Delta W)$, where $Rand$ is a uniform random number on the interval [0, 1] and $\beta = (k_B T)^{-1}$. ΔW is the energy change between the old and the new configurations based on the chosen ion k with charge q_k. In the present study, ΔW was calculated as:

$$\Delta W = W_k^{new} - W_k^{old} \tag{9}$$

$$W_k = q_k\phi_k^{stat} + q_k\phi_k^{self} + \sum_{j\neq k}\frac{q_k q_j}{\varepsilon_w}\phi^{coul}(r_{kj}) + \sum_{j\neq k} q_k q_j \phi_{kj}^{diel} + \frac{q_k q_D}{\varepsilon_w}\phi^{coul}(r_{kD}) + q_k q_D \phi_{kD}^{diel} - k_B T \ln(D_k(z)/D_k^0), \tag{10}$$

where q_j and q_D are the charges of ion j and D65, respectively. Furthermore, D_k^0 and $D_k(z)$ are the diffusion constants of an ion k in the bulk and at position z, respectively. The first term in the right hand side of Eq. 10 is the effective electrostatic potential due to charges (excluding D65) in the first extracellular domain. Electrostatic calculations (solutions of the Poisson's equation with an applied external potential $\Delta V = V_L - V_R$) were performed on a $133 \times 133 \times 165$ lattice with a lattice spacing of 0.5 Å. The second term represents the dielectric self-energy or the image potential due to the charged ion k. The third term calculates Coulombic interactions between pairs of ions in a dielectrically uniform environment characterized by the water dielectric constant ε_w, and the fourth term corresponds to the image potential experienced by ion k due to the surface charge induced by ion j. These two terms account for the ion–ion interaction in a dielectric-inhomogeneous medium. The fifth term corresponds to Coulombic interactions between residue D65 and the chosen ion k in a dielectrically uniform environment, and the sixth term contributes to the image potential experienced by ion k due to the surface charge induced by residue D65. These two terms together estimate the Coulombic interactions between ion and the charged residue D65. The effects of the dielectric inhomogeneity of the channel environment on the ion–ion and ion–D65 electrostatic interactions (the fourth and sixth terms in Eq. 10) were implemented using an efficient empirical pair potential (Cheng and Coalson, 2005; Cheng et al., 2007):

$$\phi_{kj}^{diel} = 2\sqrt{\phi_{k\leftarrow k}^{diel}\phi_{j\leftarrow j}^{diel}}\exp(-cr_{kj}/L), \tag{11}$$

where $\phi_{k\leftarrow k}^{diel}$ and $\phi_{j\leftarrow j}^{diel}$ are the dielectric contribution to the self-energy (or the image potential) for ions k and j with a unit (proton) charge. ϕ_{kD}^{diel} was also calculated using Eq. 11, with $\phi_{D\leftarrow D}^{diel}$ taken to be the image potential near the pore surface. A detailed description for calculating $\phi_{k\leftarrow k}^{diel}$ can be found in Cheng and Coalson (2005). L is the length of the channel, and r_{kj} is the distance between the ions k and j, and $c = 2.0$. Finally, the last term in Eq. 10 is included to account for the effect of the nonuniform ion diffusion constant profile, which in the model considered in this study varies only along the channel direction. The diffusion constants and the associated ion displacements taken in one DMC step obeyed the relation:

$$h_k(z)^2/D_k(z) = h_k^{02}/D_k^0, \tag{12}$$

where $h_k(z)$ and h_k^0 are the associated ion displacement at position z and bulk solution for ion k, respectively. To synchronize time between the mobile ions, the ion displacement in the bulk for different cations was related to that of chloride ion as follows:

$$h_X^{0\,2} / D_X^0 = h_{Cl}^{0\,2} / D_{Cl}^0, \tag{13}$$

where h_X^0, h_{Cl}^0 and D_X^0, D_{Cl}^0 are the bulk displacement and diffusivity for cations (X represents Li^+, Na^+, K^+, Rb^+, or Cs^+) and chloride ions, respectively. The total simulation time T_s is related to the number of the Monte Carlo cycles N_c as:

$$T_s = \frac{h_{Cl}^{0\,2} N_c}{6 D_{Cl}^0}. \tag{14}$$

Note that in our DMC method to simulate ion permeation, a hard core–excluded volume potential was also included. In particular, we did not permit overlap between an ion and the protein channel, between any two ions, or between ions and D65 residues. If an attempted move gave rise to this type of overlap, it was rejected.

The computational box (excluding the buffer region) had a size of $L_x \times L_y \times L_z = 66 \times 66 \times 82$ Å. The constructed model channel extended from $z = -16$ (Å) to $z = 16$ (Å). To our knowledge, the diffusion constant of an ion inside a protein channel has yet to be experimentally measured for any channel. On the basis of molecular dynamics investigations of diffusion constants for K^+ and Cl^- inside the OmpF porin channel (Im and Roux, 2002) and K^+ in gramicidin A (Mamonov et al., 2006), the diffusivities for different ions in claudin-2 were assumed to be linearly reduced from their bulk values near the channel entrance ($z_L = -20$ Å and $z_R = 20$ Å) to half their bulk values ($z_L = -16$ Å and $z_R = 16$ Å), and maintained at half their bulk diffusivities throughout the whole pore domain (-16 Å $< z < 16$ Å). (Note that using an internal diffusion constant of roughly half the bulk diffusion constant of permeant Na^+ and Cl^- ions in two independent Brownian dynamics simulations of ion flow through the glycine receptor, which has a pore diameter of approximately 6 Å, yielded conductance values in reasonable agreement with experiments [O'Mara et al., 2003; Cheng et al., 2005]. The radii and the bulk diffusivities of different ions were taken from Pauling [1948] and Hille [2001] and are listed in Table S4, which is available at http://www.jgp.org/cgi/content/full/jgp.200810154/DC1.) For simplification, the charged residue D65 was assumed to be fixed. In the present study, $R_D = 0.5$ Å, $R_c = 3.75$ Å, $q_D = -0.1$ (e), and $\phi_{D\leftrightarrow D}^{diel} = 3.0$ K_BT were used for D65. The displacement of Cl^- ions in the bulk was set to $h_{Cl}^0 = 0.5$ Å for all simulations. The dilution potential and biionic potential were extracted from the Brownian dynamics simulations following the same procedure used in the experimental studies.

Online Supplemental Material

In Online Supplemental Material I, we describe in detail the rationale and procedures used to correct for liquid junction potentials and studies to validate our method. In Online Supplemental Material II, we give the full details of our Brownian dynamics simulations. The physicochemical properties of mobile ions used in the simulations are listed in Table S4. Additional simulations were performed to determine the sensitivity of claudin-2 pore behavior to changes in the channel geometry, protein dielectric constants, and ion diffusivity profiles (Fig. S4 and Tables S5 and S6), and to changes in the electrostatic field strength generated from D65 (Figs. S5 and S6). In Online Supplemental Material III, we show the results of conductance measurements in the presence of different alkali metal cations. The online supplemental material is available at http://www.jgp.org/cgi/content/full/jgp.200810154/DC1.

RESULTS

Characterization of WT Claudin-2–expressing Cells

MDCK I TetOff claudin-2 cells exhibit inducible expression of mouse WT claudin-2 in the absence of doxycycline (Dox−), which was completely suppressed in the presence of doxycycline (Dox+) (Fig. 3 A). By immunofluorescence, claudin-2 was predominantly colocalized with ZO-1 at the apical junctional complex, with some additional intracellular staining (Fig. 3 B). Induction of claudin-2 did not affect the levels of the other claudins known to be expressed endogenously in MDCK I cells (Fig. 3 C), and the number of tight junction strands and the strand morphology were both found to be unchanged (Fig. 3 D). Cells induced to express claudin-2 (Dox−) had an ∼10-fold increase in transepithelial conductance (Fig. 4 A). Conductance scanning showed that claudin-2 expression markedly increased the conductance near the intercellular junctions, but not at the cell bodies, confirming that the route of claudin-2 conductance was paracellular (Fig. 5 A). The dose dependence of the claudin-2 effect was assessed by varying the concentration of doxycycline. We found that the increase in conductance mirrored claudin-2 protein levels

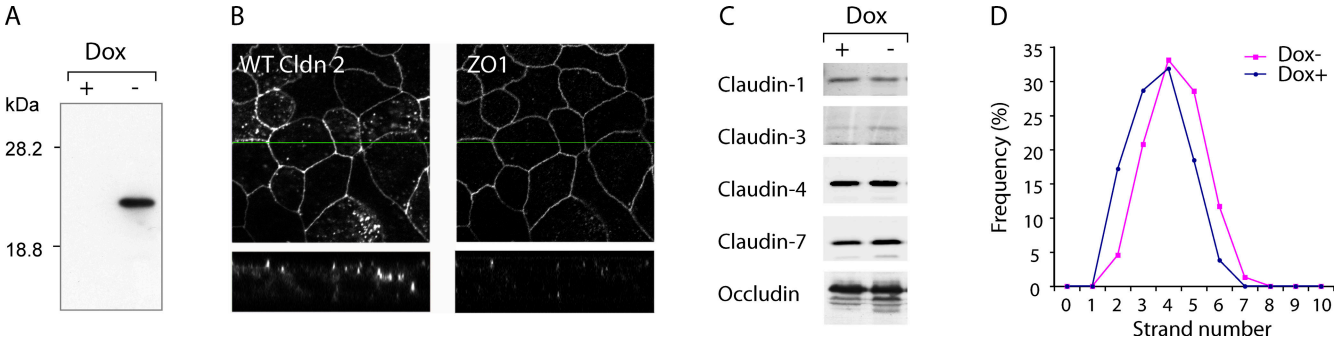

Figure 3. Characterization of MDCK I TetOff cells stably transfected with WT claudin-2. (A) Immunoblot of claudin-2 in lysate from cells grown in the presence (+) or absence (−) of doxycycline (Dox). (B) Double immunofluorescence staining of Dox− cells using an antibody to claudin-2 (left) and ZO-1 (right). En face confocal images (top) and vertical images (bottom) at the position indicated by the green line are shown. (C) Effect of claudin-2 induction on expression of other tight junction membrane proteins. Cell lysates were immunoblotted with antibodies against the indicated claudin isoforms or occludin. (D) Frequency histogram of tight junction strand counts measured in freeze-fracture replicas (154 counts per replica). Median strand number for both Dox+ and Dox− cells was 4.

(Fig. 6), consistent with the idea that the increase in conductance occurs through claudin-2 pores.

To determine the relative and absolute permeability to Na^+ and Cl^-, NaCl dilution potentials were measured (Fig. 4 B). Dilution potentials determined at different apical/basolateral NaCl activity ratios fit well to a Goldman-Hodgkin-Katz equation (Fig. 4 C). We therefore used 150 mM NaCl/75 mM NaCl dilution potentials and the Goldman-Hodgkin-Katz equation to derive relative permeabilities for Na^+ and Cl^-. Table I lists the raw data, which is summarized in Fig. 4 D. Induction of claudin-2 increased P_{Na} by ~10-fold compared with control Dox+ cells; P_{Cl} was increased approximately fourfold. By subtracting the conductance and permeability in Dox+ cells from that in Dox− cells, we derived the increase in transepithelial conductance and permeability attributable to the introduction of claudin-2–based paracellular pores (Fig. 4 E). We therefore have a quantitative measure of the macroscopic conductance and permeability of a claudin-based pore. By this method, the permeability of claudin-2 to Na^+ was determined to be 7.5 ± 0.9 times its permeability to Cl^-. Thus, claudin-2 forms cation-selective pores. Furthermore, these pores appear to be nonrectifying and exhibit a fairly linear relationship between conductance and Na^+ concentrations varied within the physiological range, without evidence of saturation (Fig. 5, B and C). The apparently linear conductance–concentration relationship makes it unlikely that a surface charge effect is the cause of the Na^+ selectivity.

What is the basis for the cation selectivity of claudin-2? To investigate the interaction between permeating cations and the claudin-2 pore, we determined the permeability of claudin-2 to other alkali metal cations using biionic potentials (Fig. 7 A and Table I). The permeability sequence was found to be: $K^+ > Rb^+ > Na^+ > Li^+ >> Cs^+$. This sequence is quite different from the sequence of their free-solution mobilities and resembles Eisenman selectivity sequence V–VIII. This suggests that permeating cations have to dehydrate to enter the claudin-2 pore, and that there must be a moderately high field strength, negatively charged interaction site within the pore that stabilizes the dehydrated cation (Diamond and Wright, 1969; Eisenman and Horn, 1983). This would also explain the high selectivity for cations over anions. However, the ratio between the permeabilities of the most permeable cation (K^+) and the least permeable (Cs^+) was 1.6, which is quite narrow and suggests that the interaction site is partially hydrated. To assess the size of the claudin-2

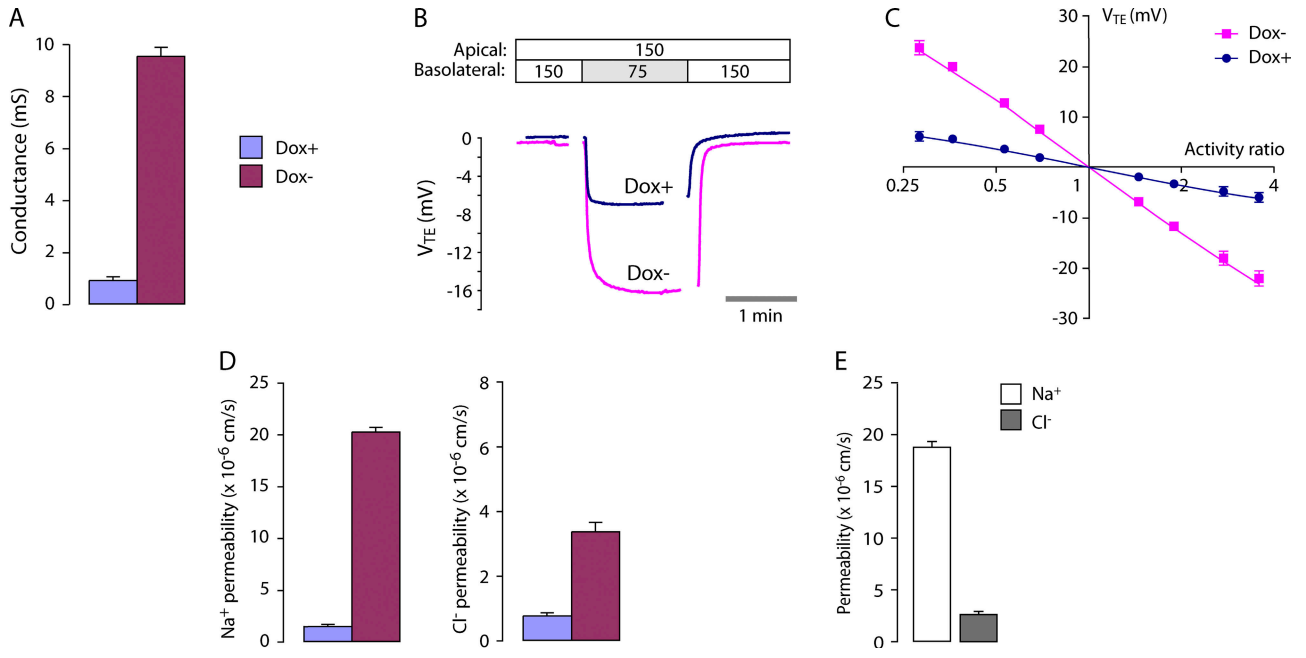

Figure 4. Conductance and NaCl permeability of the WT claudin-2 pore. (A) Transepithelial conductance in MDCK I TetOff cells that were either uninduced (Dox+) or induced to express WT claudin-2 (Dox−). Columns show mean ± SE (n = 3 monolayers in a single experiment) and are representative of four independent experiments. (B) Raw voltage traces, V_{TE} (apical with reference to basolateral), acquired in a typical NaCl dilution potential experiment. The NaCl concentrations of the Ringer solutions on each side of the monolayers are shown at the top (in mM). Gaps in acquisition occurred during solution exchange. (C) Determination of relative permeability from NaCl dilution potentials. The transepithelial diffusion potential, V_{TE}, was determined at different NaCl activity ratios (apical activity/basolateral activity) and plotted on a log-linear scale. Data were fit by nonlinear regression to the Goldman-Hodgkin-Katz equation with best-fit values (95% CI) for P_{Na}/P_{Cl} of 1.5 (1.4–1.6) for Dox+ and 6.3 (5.7–6.8) for Dox−. (D) Permeability to Na^+ and Cl^- in Dox+ and Dox− cells, determined from dilution potential measurements (see A for color code). (E) Apparent permeability of the claudin-2 pore to Na^+ and Cl^-, determined by subtracting measurements in Dox+ cells from those in Dox− cells.

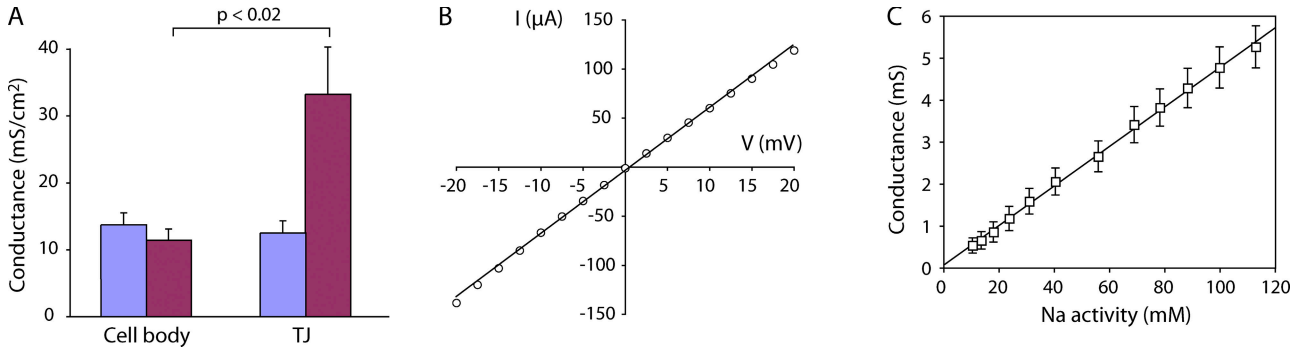

Figure 5. Characteristics of the WT claudin-2 pore conductance. (A) Conductance scanning to distinguish the effect of claudin-2 on transcellular from paracellular conductance. Transcellular conductance was determined by scanning above the cell body, and paracellular conductance was determined by scanning over the lateral cell border (TJ). Results show the mean of 12–15 conductance measurements per site performed on two filters each. (B) Relationship between transepithelial voltage (V) and the current (I) carried by claudin-2. (C) Relationship between extracellular Na^+ activity and claudin-2 conductance. Na^+ concentration was adjusted by isosmotic replacement of NaCl with mannitol.

pore, its permeability to three organic cations, methylamine, ethylamine, and tetramethylammonium, was determined and fit to a Renkin equation (Fig. 7 B and Table II). The pore diameter estimated by nonlinear regression was 6.5 ± 0.3 Å. This is smaller than the diameter of a hydrated Na^+ ion, 7.2 Å (Nightingale, 1959), so that Na^+ would likely have to shed at least part of its hydration shell to permeate through the claudin-2 pore, consistent with the predictions of the alkali metal Eisenman sequence.

A protein can form a negatively charged site from fixed net charges or partial charges from dipoles. When the pH of the extracellular fluid was lowered, claudin-2 conductance fell promptly, at a rate (time constant 8.2 ± 0.02 s) similar to that of solution mixing in our Ussing chambers, suggesting a diffusion-limited process (Fig. 7 C). Moreover,

TABLE I

Alkali Metal Cation Diffusion Potential Measurements and Calculations of Permeability

	WT				E53Q				D65N				D76N				TM			
	Dox+		Dox−		Dox+		Dox−		Dox+		Dox−		Dox+		Dox−		Dox+		Dox−	
	Mean	SE	Mean	SE	Mean	SD	Mean	SE	Mean	SE	Mean	SE	Mean	SE	Mean	SE	Mean	SE	Mean	SE
Conductance (mS)	0.90	0.08	9.52	0.20	0.32	0.03	10.43	0.13	0.79	0.04	3.87	0.04	0.51	0.05	9.10	0.34	0.42	0.01	2.76	0.24
2:1 NaCl dilution potential (mV)[a]	−5.43	0.38	−11.93	0.41	−0.30	0.80	−12.33	0.70	−2.77	0.38	−9.56	0.63	−3.47	0.87	−12.05	0.43	2.62	0.40	−6.74	0.26
Biionic potentials (mV)[a]																				
LiCl	−2.31	0.52	−1.73	0.42	−3.17	0.30	−2.36	0.27	−4.35	0.33	−7.57	0.30	−2.42	0.43	−2.30	0.82	−3.02	0.35	−7.07	0.24
KCl	4.78	0.53	4.98	0.46	4.47	0.69	5.63	0.50	5.32	0.52	6.04	0.42	4.92	0.51	4.91	0.44	5.17	0.61	5.71	0.29
RbCl	3.31	0.28	2.07	0.49	4.79	0.54	2.17	0.46	4.83	0.56	3.54	0.23	4.23	0.53	2.35	0.59	5.95	0.66	3.75	0.25
CsCl	−0.74	0.24	−5.46	0.58	3.87	0.24	−6.91	0.50	2.60	0.39	−1.75	0.32	1.73	0.58	−4.73	0.72	5.48	0.56	−0.77	0.23
Relative permeabilities																				
P_{Na}/P_{Cl}	1.99	0.10	6.11	0.55	1.05	0.10	6.98	1.08	1.41	0.07	3.79	0.39	1.56	0.16	6.32	0.62	0.73	0.04	2.39	0.09
P_{Li}/P_{Na}	0.88	0.03	0.93	0.02	0.78	0.02	0.90	0.01	0.74	0.02	0.69	0.01	0.86	0.03	0.90	0.03	0.74	0.04	0.67	0.01
P_K/P_{Na}	1.29	0.03	1.24	0.03	1.37	0.08	1.27	0.03	1.38	0.05	1.32	0.03	1.34	0.05	1.24	0.03	1.51	0.08	1.34	0.02
P_{Rb}/P_{Na}	1.20	0.01	1.10	0.02	1.39	0.06	1.10	0.02	1.34	0.05	1.18	0.02	1.29	0.05	1.11	0.03	1.60	0.09	1.21	0.02
P_{Cs}/P_{Na}	0.96	0.01	0.79	0.02	1.31	0.03	0.74	0.01	1.18	0.03	0.92	0.01	1.11	0.04	0.81	0.02	1.55	0.08	0.96	0.01
Absolute permeabilities (× 10^{-6} cm/s)																				
P_{Na}	1.47	0.11	20.21	0.50	0.40	0.04	22.43	0.25	1.14	0.06	7.55	0.12	0.75	0.05	19.38	0.45	0.43	0.01	4.80	0.41
P_{Li}	1.30	0.14	18.72	0.61	0.31	0.03	20.24	0.50	0.85	0.07	5.19	0.17	0.65	0.05	17.50	0.30	0.32	0.02	3.22	0.32
P_K	1.90	0.11	25.04	0.64	0.54	0.06	28.50	0.51	1.57	0.07	9.99	0.21	1.01	0.08	23.97	1.09	0.66	0.03	6.42	0.48
P_{Rb}	1.76	0.12	22.12	0.62	0.55	0.06	24.62	0.43	1.53	0.07	8.91	0.11	0.97	0.09	21.50	1.09	0.69	0.03	5.83	0.47
P_{Cs}	1.41	0.09	15.86	0.42	0.52	0.06	16.55	0.34	1.34	0.06	6.95	0.08	0.84	0.07	15.78	0.84	0.67	0.03	4.61	0.40
P_{Cl}	0.75	0.10	3.36	0.29	0.39	0.05	3.39	0.57	0.81	0.05	2.03	0.20	0.50	0.09	3.15	0.41	0.60	0.02	2.02	0.19

Data have been corrected for filter and fluid resistance and for liquid junction potentials as described in the online supplemental material and are representative of one experiment, showing the mean and standard error of three monolayers each.

[a]Diffusion potentials are measured on the side containing 150 mM NaCl, relative to the side with 75 mM NaCl (dilution potential) or 150 mM XCl (biionic potentials).

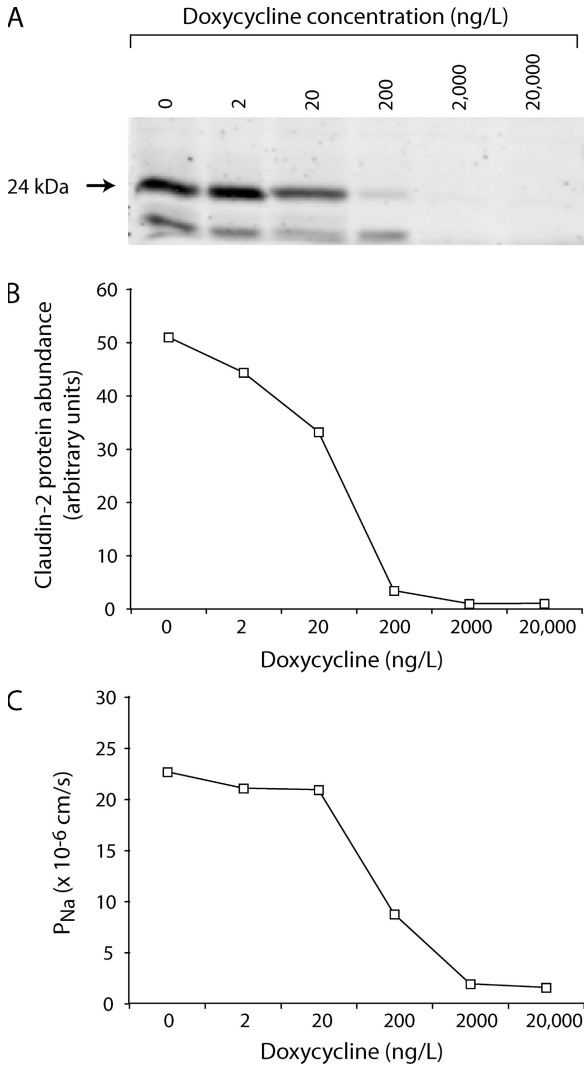

Figure 6. Dose–response relationship between claudin-2 protein level and Na^+ permeability. (A) Immunoblot showing expression of WT claudin-2 (24 kD band) induced (no doxycycline) or suppressed with varying concentrations of doxycycline. (B) Quantitation of immunoblot bands to assess claudin-2 protein abundance. (C) Permeability to Na^+ (P_{Na}), as determined by NaCl dilution potential measurement.

the acidification-induced reduction in conductance was due predominantly to a reduction in the Na^+ permeability of claudin-2 (Fig. 7 D), with no apparent change in Cl^- permeability. This suggests that acidification is titrating and neutralizing fixed net negative charge(s) at the cation interaction site. Consistent with this, the relationship between pH and conductance could be fit to a single-site model with a Hill coefficient of 1.0 and a pK_a of 4.9 ± 0.1, which is well within the pK_a range for the side chain carboxylate groups of acidic amino acid residues (Fig. 7 E).

Characterization of Cells Expressing Charge-neutralizing Mutants of Claudin-2

Anderson, van Itallie, and colleagues have used charge-reversing mutations that alter paracellular charge selectivity to show convincingly that the first extracellular domain of claudins lines the paracellular pore (Colegio et al., 2002, 2003; Van Itallie et al., 2003). However, it is unclear whether these mutants also inform on the location of the ion selectivity filter or merely reflect artificially created electrostatic fields within the pore that affect ion permeation. Indeed, the fact that mutations of most charged residues in the first extracellular domain have a similar effect would suggest the latter. There are three acidic residues in the first extracellular loop of claudin-2: E53, D65, and D76. To test the hypothesis that one or more of these might be responsible for the negatively charged cation-interaction site in the claudin-2 pore, we mutated each of these to its neutral, polar counterpart (E53Q, D65N, and D76N), generated a triple mutant (TM) bearing all three mutations, and generated stable, inducible MDCK I TetOff cell lines expressing each mutant. By neutralizing instead of reversing the normal charge at each site, we expect to pinpoint only those residues that are part of the normal selectivity mechanism. Clones were selected that expressed similar levels of claudin-2 protein to WT and showed good induction and suppression. Mutant cell lines exhibited similar levels of expression and subcellular localization of claudin-2 protein to the WT claudin-2 clone, and similarly had little effect on expression of endogenous claudins (Fig. 8).

When the conductance and Na^+ and Cl^- permeability of the mutant claudin-2 proteins were measured, E53Q and D76N were found to be very similar to WT claudin-2 (WT). However, D65N exhibited threefold lower conductance and Na^+ permeability, with no change in Cl^- permeability, and the TM was indistinguishable from D65N (Fig. 9, A and B). Thus, D65 is required for maximum cation permeability of claudin-2. The temperature dependence of conductance and Na^+ permeability was measured and fit to the Arrhenius equation to determine the activation energy of permeation (E_a). Mutation of D65 to N increased the activation energy for conductance (41.8 ± 4.3 kJ/mol vs. 39.7 ± 1.9 kJ/mol for WT) and P_{Na} (42.7 ± 2.0 kJ/mol vs. 39.0 ± 1.4 kJ/mol for WT) (Fig. 9, C and D). The observed changes of 2–4 kJ/mol are the right order of magnitude to account for the permeability changes (an e-fold reduction in P_{Na} would be expected with an increase in the height of the energy barrier of $1RT$ = 2.6 kJ/mol) and suggest that D65N in some way impedes the kinetics of Na^+ permeation, rather than reducing the number of available pores. Furthermore, the permeability pattern of organic cations and estimated pore diameter (5.8 ± 0.3 Å) of D65N was not significantly different from that of WT claudin-2 (Fig. 7 B), excluding steric hindrance as the explanation. Thus, the most likely explanation is that D65 forms part of the electrostatic cation interaction site.

Three independent experiments suggest that D65 is part of the negatively charged interaction site. First, we

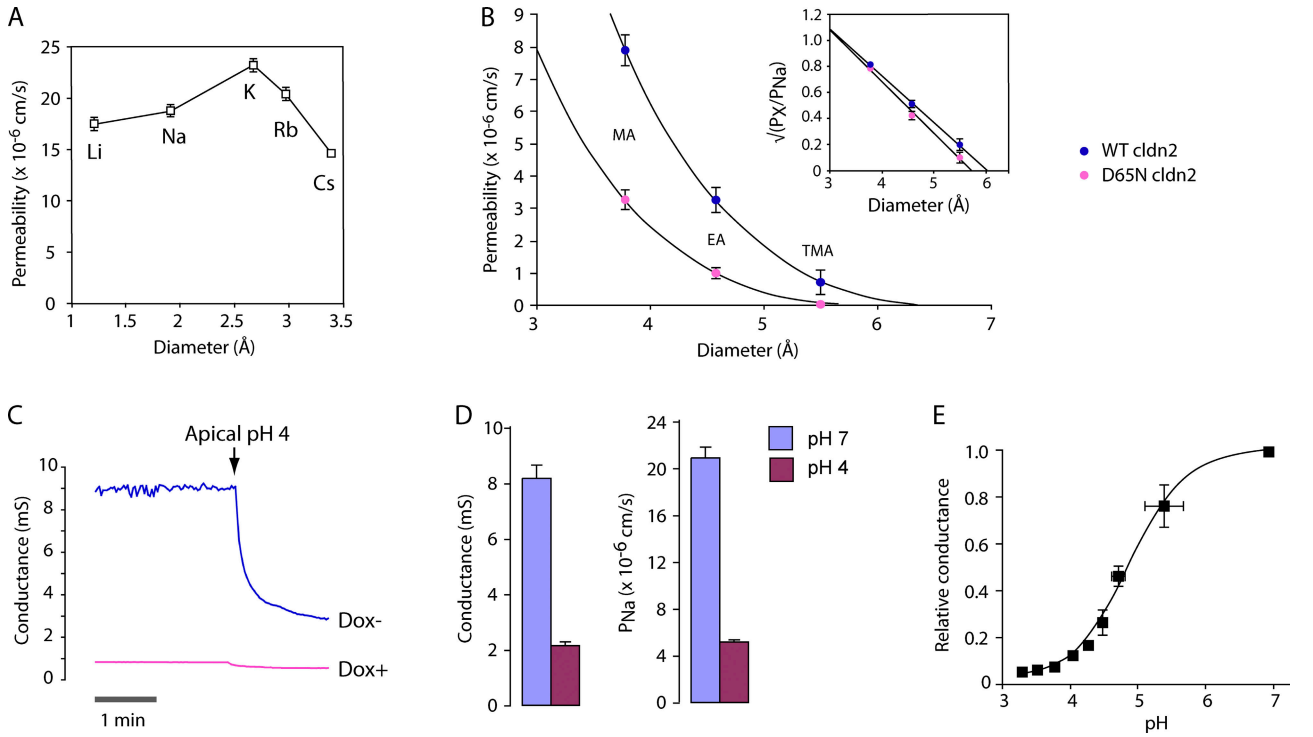

Figure 7. Biophysical properties of the WT claudin-2 pore. (A) Permeability of WT claudin-2 to alkali metal cations, as determined by biionic potentials. (B) Estimation of pore size. The permeability of WT and D65N claudin-2 to organic cations (P_X) was calculated from biionic potentials. Curves were fit by nonlinear regression to a Renkin equation with pore diameter, *D*, of 6.5 ± 0.3 Å (WT) and 5.8 ± 0.3 Å (D65N). MA, methylamine; EA, ethylamine; TMA, tetramethylammonium. (Inset) Data are replotted as $\sqrt{(P_X/P_{Na})}$ versus diameter to show linear fit. (C) Conductance trace showing the effect of acidification of the apical compartment to pH 4.0 on cells expressing WT claudin-2. (D) Summary of effect of acidification to pH 4.0 on conductance and P_{Na} of WT claudin-2. (E) Effect of acidification to different pH on conductance, G, relative to that at pH 7. The curve shows the fit to a Hill equation, $G = G_{max}\{(K_a + \alpha[H^+]^n)/(K_a + [H^+]^n)\}$, where G_{max} is the maximum conductance, K_a is the equilibrium constant, n is the Hill coefficient, and α is a proportionality constant. Best-fit values were $n = 1.0$ and $pK_a = 4.9 \pm 0.1$.

were able to demonstrate by radiotracer flux assay that Ca^{2+} passes through WT claudin-2 pores with a permeability approximately fourfold lower than Na^+. If D65 is an electrostatic interaction site for permeating cations, one would expect abolition of the net charge to have a disproportionately large effect on the permeability of polyvalent, compared with monovalent, cations. Indeed, whereas $P_{Na}(WT)/P_{Na}(D65N)$ was 2.9 ± 0.1, $P_{Ca}(WT)/P_{Ca}(D65N)$ was 22.1 ± 0.8, indicating that loss of the carboxylate side chain of D65 disproportionately inhibits Ca^{2+} permeation (Fig. 10 A).

Second, we determined the alkali metal cation permeability sequence for all the mutants. E53Q and D76N exhibited high permeabilities to all the alkali metal cations, and the selectivity was identical to WT. D65N and TM, however, both showed substantially lower permeabilities to all the alkali metal cations and, more importantly, a differently shaped selectivity profile (Fig. 10 C). To control for the large differences in overall permeability, we normalized all the values for each mutant to its P_{Na} and plotted the relative permeabilities of each cation, X^+, as P_X/P_{Na} (Fig. 10 D). Now one can see that the relative permeabilities for most of the cations for all the mutants were very similar, with the exception of Li^+. The relative permeability to Li^+, P_{Li}/P_{Na}, was ~1 for WT, E53Q, and D76N. However, D65N and TM exhibited markedly lower P_{Li}/P_{Na}; their curves were completely superimposable, and the predicted selectivity sequence was $K^+ > Rb^+ > Na^+ > Cs^+ >> Li^+$ (Eisenman sequence V). Li^+ is the smallest and hence most strongly hydrated alkali metal. In order for Li^+ to permeate a narrow pore such as claudin-2, the huge energy cost of dehydration must be offset by an energetically favorable interaction with a site within the pore. Inspection of Eisenman's sequences shows that as the field strength of an electrostatic interaction site decreases, the first consequence is that the relative position of Li^+ is progressively demoted. Thus, the relative permeability of Li^+ is a highly sensitive marker of the field strength of an intrapore electrostatic interaction site, and its reduction in D65N and TM strongly supports the notion that the side chain of D65 is part of such a site.

Third, we showed that acidification to pH 4.0 markedly reduced the conductance of E53Q and D76N to the same extent as WT, whereas D65N and TM showed much less inhibition, suggesting loss of a titratable, negatively

TABLE II

Organic Cation Diffusion Potential Measurements and Calculations of Permeability

		WT				D65N			
		Dox+		Dox−		Dox+		Dox−	
	Mean diameter (Å)[a]	Mean	SE	Mean	SE	Mean	SE	Mean	SE
Conductance (mS)		0.82	0.07	6.20	0.22	1.30	0.10	3.59	0.26
2:1 NaCl dilution potential (mV)[b]		−2.12	0.47	−11.68	0.30	−0.33	0.22	−9.09	0.19
Biionic potentials (mV)[b]									
Methylamine		1.67	0.14	−2.42	0.28	2.07	0.15	−1.55	0.35
Ethylamine		−1.19	0.25	−8.08	0.39	−0.67	0.26	−6.96	0.47
TMA		−3.20	0.36	−11.84	0.43	−2.55	0.30	−10.05	0.53
TEA		−4.18	0.29	−12.03	0.41	−3.50	0.25	−10.10	0.49
Arginine		−4.07	0.35	−10.60	0.52	−3.21	0.31	−8.81	0.60
NMDG		−4.77	0.41	−11.18	0.19	−3.73	0.28	−8.79	0.64
Relative permeabilities									
P_{Na}/P_{Cl}		1.33	0.08	5.94	0.42	1.04	0.03	3.45	0.11
$P_{Methylamine}/P_{Na}$		1.11	0.02	0.70	0.02	1.19	0.02	0.75	0.03
$P_{Ethylamine}/P_{Na}$		0.75	0.03	0.31	0.02	0.80	0.03	0.33	0.03
P_{TMA}/P_{Na}		0.52	0.03	0.09	0.03	0.55	0.04	0.13	0.03
P_{TEA}/P_{Na}		0.41	0.02	0.08	0.02	0.43	0.03	0.12	0.03
$P_{Arginine}/P_{Na}$		0.40	0.04	0.16	0.04	0.47	0.04	0.19	0.04
P_{NMDG}/P_{Na}		0.32	0.05	0.12	0.02	0.41	0.04	0.19	0.04
Absolute permeabilities ($\times 10^{-6}$ cm/s)									
P_{Na}	1.90	1.14	0.08	13.03	0.45	1.64	0.12	6.86	0.47
$P_{Methylamine}$	3.78	1.28	0.11	9.16	0.55	1.96	0.17	5.23	0.47
$P_{Ethylamine}$	4.58	0.87	0.08	4.12	0.45	1.33	0.14	2.33	0.29
P_{TMA}	5.50	0.59	0.06	1.30	0.40	0.94	0.11	0.93	0.22
P_{TEA}	6.58	0.46	0.04	1.16	0.39	0.74	0.09	0.90	0.20
$P_{Arginine}$	6.96	0.54	0.08	2.24	0.64	0.84	0.09	1.34	0.28
P_{NMDG}	7.29	0.44	0.07	1.73	0.29	0.72	0.08	1.35	0.30

Data have been corrected for filter and fluid resistance and for liquid junction potentials as described in the online supplemental material and summarize several independent experiments ($n = 12$ monolayers, except for arginine and NMDG biionic potentials, where $n = 6$).

[a]The mean diameter of the alkali metal cations is defined as twice the Pauling radius of the nonhydrated ion. The mean diameter of the organic cations, derived from the data of Dwyer et al. (1980), is defined as the geometric mean of the dimensions of a rectangular box that would contain the ion as determined using Corey-Pauling-Koltum space-filling molecular models.

[b]Diffusion potentials are measured on the side containing 150 mM NaCl, relative to the side with 75 mM NaCl (dilution potential) or 75 mM NaCl/75 mM XCl (biionic potentials).

charged site (Fig. 10 B). Examination of alkali metal selectivity revealed that acidification of WT claudin-2 showed a trend to reduce relative Li^+ permeability, consistent with titration of the negative charge on the interaction site (Fig. 10 E). Finally, when D65 was mutated to N and acidified to pH 4, the magnitude of the reduction in Li^+ permeability was the same as with either D65N or acidification alone; in other words, there was no additive effect. This is consistent with the hypothesis that the functional consequence of acidification was caused by titration of the side chain carboxylate of D65.

Brownian Dynamics Modeling of Claudin-2 Pore Behavior

Further evidence in support of the mechanism for charge and alkali metal selectivity of claudin-2 was obtained by using Brownian dynamics simulations to model the behavior of the pore. We used a simple model in which the pore was assumed to be a 6.5-Å diameter cylinder with conical vestibules and the negatively charged side chain of aspartate-65 positioned at the center and facing into the lumen (Fig. 11 A). Because claudins are likely multimeric and possibly hexameric, we assumed that D65 contributed six identical partial charges. The claudin-2 pore shows no obvious current rectification, so we further assumed that D65 is located in the middle of the selectivity filter to avoid possible current rectification arising from asymmetry of the channel geometry and fixed charge location. Referring to the (symmetric) channel geometry presented in Fig. 11 A, placing D65 5 Å away from the channel center toward the left channel entrance induced a slight current rectification characterized by $\gamma_{+40mv}/\gamma_{-40mv} = 1.25$ because more cations were attracted into the channel entrance from the left side (at +40 mV) than from the right side (at −40 mV).

As expected, this simple model was sufficient to reproduce the high degree of cation selectivity of the pore. This model pore exhibited P_{Cl}/P_{Na} of 0.07 ± 0.03

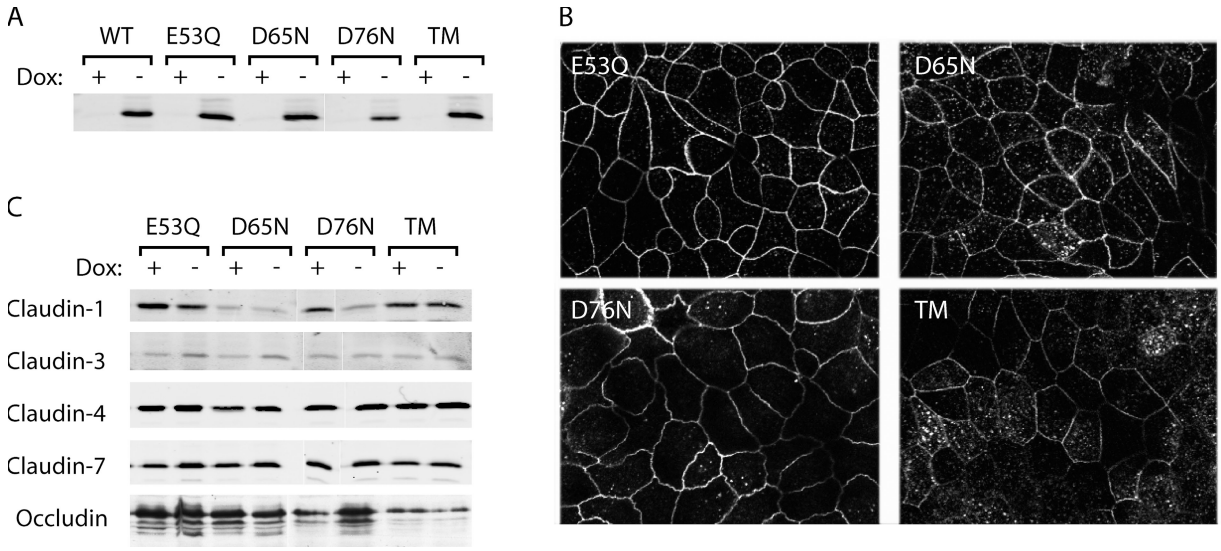

Figure 8. Characterization of MDCK I TetOff cell lines expressing charge-neutralizing mutants of claudin-2. (A) Immunoblot of claudin-2 expression in clones stably transfected with WT claudin-2 (WT), the indicated individual claudin-2 mutants, and a TM (TM = E53Q, D65N, and D76N) grown in the presence (+) or absence (−) of doxycycline (Dox), using antibodies to the indicated claudin isoforms. (B) Confocal images showing immunofluorescence localization of mutant claudin-2 protein in Dox− cells. (C) Effect of claudin-2 induction on expression of other tight junction membrane proteins. Cell lysates were immunoblotted with antibodies against the indicated claudin isoforms or occludin. (A and C) White lines indicate that intervening lanes have been spliced out.

and a linear current–voltage relationship (Fig. 11 B). Neutralizing the charge on D65 (equivalent to the D65N mutation) reduced Na permeability by ∼2/3. Additionally, it was able to discriminate between the behaviors of different alkali metal cations to a certain degree based on the different sizes and the different diffusivity profiles of the various permeating cations. Thus, the model closely resembles our experimental results.

Our model explains why we observed a linear conductance–concentration profile (Fig. 5 C) instead of a saturating function, as would be expected with an Na^+ binding site. Our model predicts that saturation does in fact occur, but only at very high Na^+ concentrations (half-maximal conductance at an Na^+ activity of 600 mM), so that the relationship appears pseudolinear at the physiological Na^+ concentrations used in

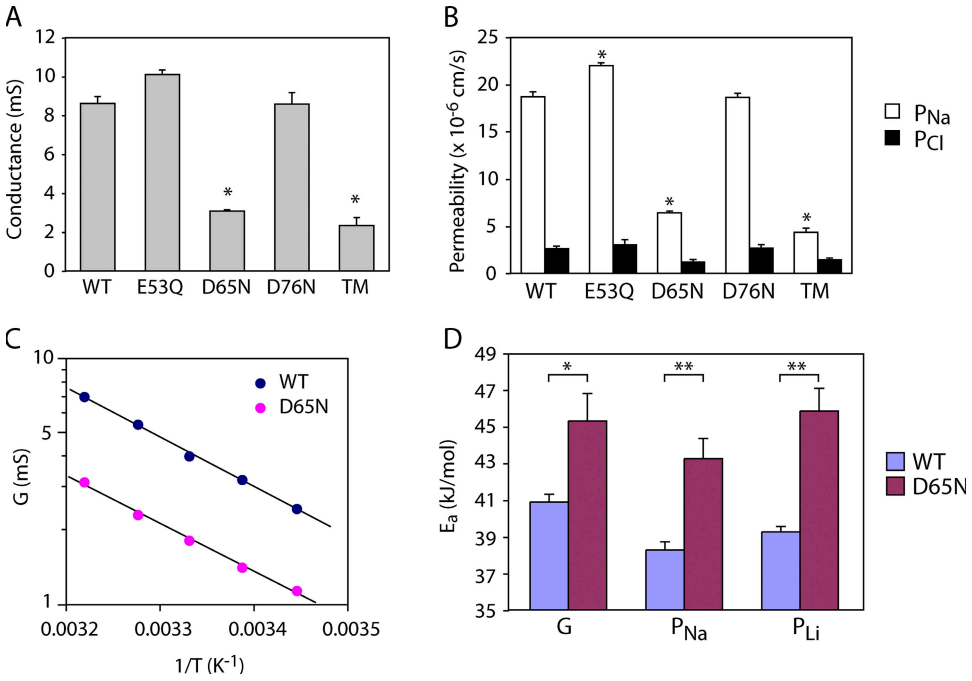

Figure 9. Effect of charge-neutralizing mutations in the first extracellular domain on claudin-2 permeability. (A and B) Conductance and Na^+ and Cl^- permeability of claudin-2 WT (WT) and mutants (TM = E53Q, D65N, and D76N). *, $P < 0.001$ compared with WT. (C) Arrhenius plot showing the relationship between conductance (log scale) and the reciprocal of the absolute temperature (T). (D) Activation energies (E_a) for conductance and permeability to Na^+ and Li^+, determined by linear regression from Arrhenius plots. *, $P < 0.05$; **, $P < 0.01$.

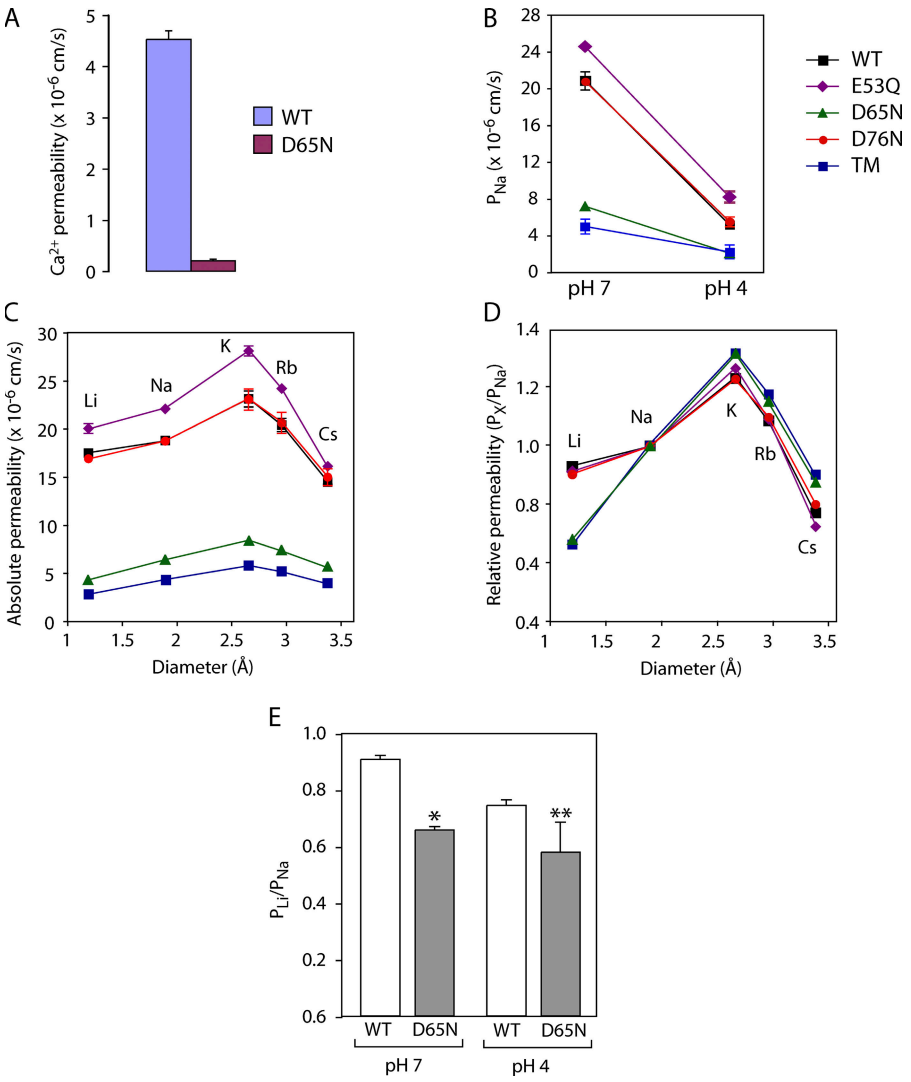

Figure 10. Evidence that aspartate-65 is an electrostatic cation interaction site. (A) Effect of D65N on permeability to Ca^{2+}, as measured by radiotracer flux assay. (B) Effect of acidification to pH 4.0 on P_{Na} of WT and mutant claudin-2. (C and D) Absolute and relative permeabilities to alkali metal cations of WT and mutant claudin-2 (see B for explanation of symbols). (E) Relative permeability to Li^+ (P_{Li}/P_{Na}) of WT or D65N claudin-2 at pH 7.0 or 4. *, $P < 0.01$; **, $P < 0.001$ compared with WT at pH 7.0 ($n = 6$–9).

our experiments (Fig. 11 C). The model also allows us to estimate the conductance of a single claudin-2 pore over a range of Na^+ concentrations. At a concentration of 150 mM Na^+, the conductance was ~70 pS, and at saturation it was 450 pS.

Fig. 11 D shows the sequence of cation selectivity predicted by the Brownian dynamics model developed herein, which bears a respectable similarity to the corresponding experimental curve shown in Fig. 7 A. It is not obvious a priori that such a model can distinguish between cations of the same valence, and indeed previous discussions have expressed pessimism concerning the flexibility of Brownian dynamics simulations in this regard (Corry et al., 2005). The primary differences between, say, an Na^+ ion and a Cs^+ ion in this type of simulation are the radius of the bare ion and its bulk diffusivity. Thus, there are two competing effects in our numerical models that determine the relative permeability ratio among different alkali cations. (1) Ion diffusivity profiles. Assuming the same ion size for all alkali cations, the relative permeability ratio among different cations will be K, Cs, Rb > Na > Li, based on bulk ion diffusivities (Pauling, 1948) (compare Table S4). (2) Entropic effects (i.e., excluded volume effect). Assuming the same ion diffusivity profiles for all cations (compare Table S6, model 4), the relative permeability ratio among different cations is Li > Na > K > Rb > Cs. Our results show that relatively small differences in cation radius can result in detectable differences in selectivity when the geometric features of the channel, dielectric and diffusion constants for the ions, etc., are chosen appropriately. It should be noted, however, that our simple model is unsuccessful in one respect: when the negative charge on the D65 residue is abolished, the relative permeability plot remains qualitatively similar to that shown in Fig. 11 D for the anionic D65 case. That is, the relative permeability of Li^+ does not decrease in the Brownian dynamics simulations as it does experimentally (compare Fig. 10 D). This failure may be due to the highly simplified rendering of the D65 residue adopted here, as noted in Discussion below.

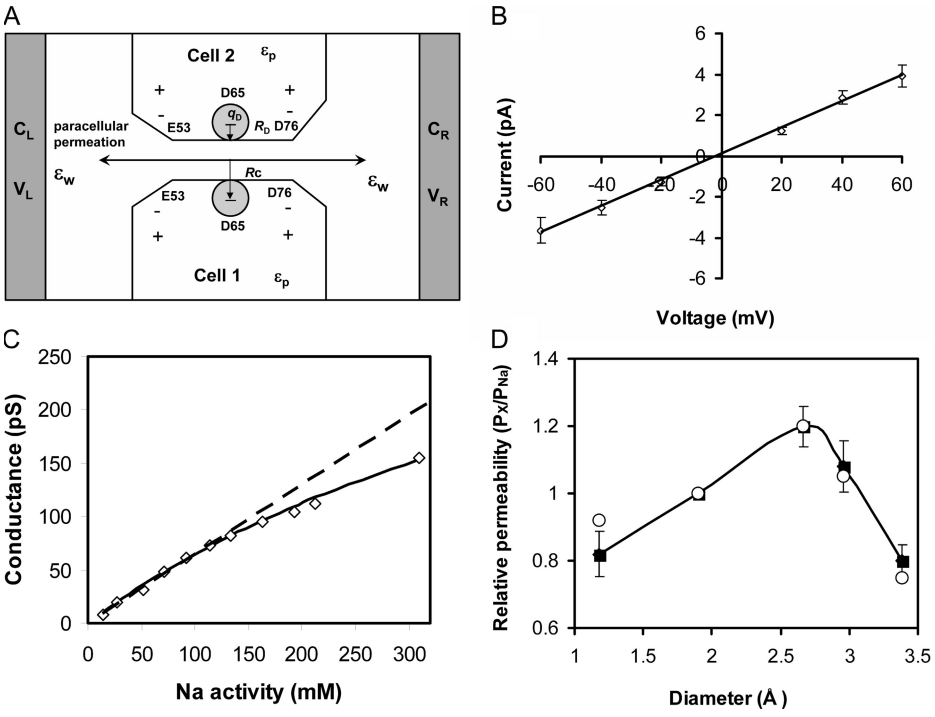

Figure 11. Brownian dynamics modeling of the claudin-2 pore. (A) Model of the WT claudin-2 pore. E53 and D76 are positioned near the pore entrances. Residue D65 is placed in the middle and represented by a charged sphere characterized by its size R_D, charge q_D, and the distance between the pore centerline and the sphere center, R_C. (B) Current–voltage relationship obtained in symmetric 150 mM NaCl. Open symbols with error bars represent numerical simulation data. (C) Conductance–concentration profile obtained from simulations with symmetrical NaCl concentrations up to 450 nM. Data points within the experimental range (up to a Na^+ activity of 113 mM or concentration of 150 mM) are fit by a dashed line. The solid line shows a curve fit of the entire dataset to the Michaelis-Menten equation: $G = G_{max}/(1 + Na_s/[Na])$, where G_{max} = 450 pS and Na_s = 600 mM. (D) Alkali metal cation selectivity (displayed as permeability relative to that of Na^+) determined by the biionic potentials obtained in our numerical simulations (shown as filled squares with error bars). For comparison, the experimental values (from Fig. 7 A) are shown as open circles.

DISCUSSION

Here, we determine the transepithelial conductance and permeability of MDCK I cells induced to express claudin-2 and subtract it from measurements done in the control, uninduced state. We suggest that this yields a quantitative measure of the macroscopic conductance and cation permeability of claudin-2–based pores. Our reasoning is supported by three observations. First, claudin-2 induction does not alter the number of tight junction strands. Thus, claudin-2 pores are presumably inserted into existing strands, and their conductance would be expected to be additive over the background conductance. Second, claudin-2 does not substantially alter the expression of other known endogenous tight junction membrane proteins (claudins 1, 3, 4, and 7, and occludin). Thus, changes in paracellular permeability are probably not confounded by changes in endogenous tight junction proteins, although we cannot exclude the possibility that other as yet unidentified endogenous claudins could be affected. We currently do not have a structural explanation of how "extra" claudin molecules can insert into existing strands without displacing endogenous tight junction proteins. Third, the conductance of overexpressed claudin-2 is very high compared with the baseline transepithelial conductance of MDCK I cells, so that the signal to noise ratio is high. This means that even if claudin-2 did subtly alter the composition or arrangement of endogenous tight junction strands, any such effects on conductance would be small relative to the conductance increase due to the insertion of claudin-2 pores, and so the accuracy of our measurements should not be significantly compromised.

It is generally assumed that paracellular pores are wide and fairly nonselective. However, we find that claudin-2 is narrow (~6.5 Å diameter), and cation selective (P_{Na}/P_{Cl} = 7.5). There are inherent limitations in any method to estimate pore diameter. We chose to use cations as size probes because we wished to know the effective size of the pore for cation permeation. However, there are only a few small nitrogenous organic cations. Moreover, the chemical characteristics, and particularly the availability of groups for hydrogen bonding, of different nitrogenous cations are quite different. To the extent that this may affect interactions with the pore wall, their permeability is not a pure function of size. Thus, it is reassuring to find that our estimate is not dissimilar from that of Van Itallie et al. (2008), who used noncharged polyethylene glycols as size probes and recently reported that claudin-2 forms size-restrictive pores of ~8 Å in diameter. They also found a small size-independent component of permeability; consistent with this, we have found that even very large cations exhibit low but detectable levels of permeability through

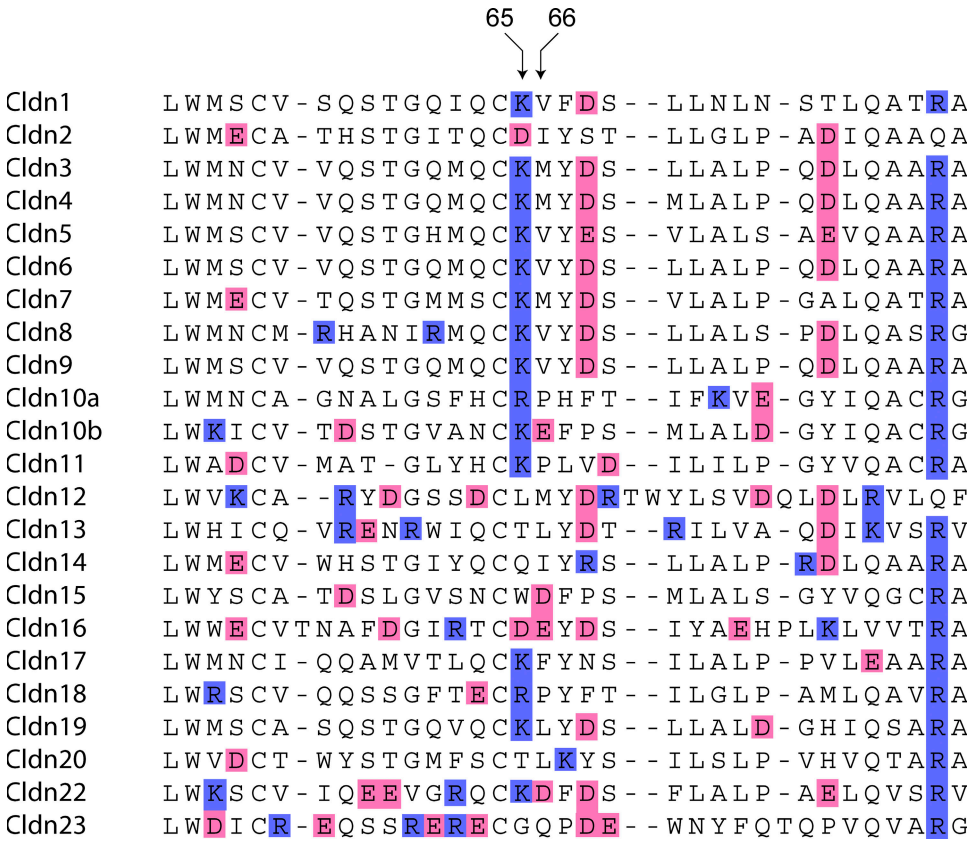

Figure 12. Alignment of the amino acid sequences of the predicted first extracellular domain of the known mouse claudin isoforms using Clustal-W. Acidic residues are shaded pink, and basic residues are shaded blue. Residues that align at the homologous position to amino acids 65 and 66 of claudin-2 are indicated by arrows.

claudin-2 (Table II). The identity of this larger permeation pathway remains unclear.

The mechanism for the remarkable cation selectivity of claudin-2 is likely to be the presence of a negatively charged electrostatic binding site that interacts with partially dehydrated permeating cations. This is based on the finding that the permeability of alkali metal cations follows a high-order Eisenman sequence, and that the cation selectivity is abrogated by extracellular acidification. Acidification could of course be acting allosterically at a distant site to alter claudin-2 conformation and hence permeability. However, the finding that acidification reduces P_{Li}/P_{Na} and changes the alkali metal selectivity to a lower-order Eisenman sequence strongly suggests that it is titrating the negatively charged binding site. The suggestion that this is an intrapore site and not a surface charge is also supported by the finding of a linear conductance–concentration relationship. At low Na^+ concentrations and hence low ionic strength, screening of any surface charges by the bulk solution is minimized and the local Na^+ concentration at the pore entrance would be increased (Green and Andersen, 1991). This would be expected to result in anomalously high conductance at low Na^+ concentrations. Instead, we observe a linear relationship, suggesting that the negatively charged site is within the pore.

Our charge-neutralizing mutations show convincingly that D65 is an important contributor to this binding site, whereas the other acidic residues in the first extracellular domain, E53 and D76, are not. The role of the first extracellular domain in determining charge selectivity of claudins has already been firmly established (Colegio et al., 2002, 2003; Van Itallie et al., 2003, 2006). However, our findings differ substantially from those of James Anderson's group. Van Itallie, Colegio, and colleagues used analysis of the number of charged residues in WT claudins, and the effect of charge-reversing mutations to indicate that charge selectivity depends on the additive effect of all the charged residues in the second half of the first extracellular loop (Colegio et al., 2002; Van Itallie et al., 2003). This would suggest a mechanism in which the general electrostatic environment within the pore determines charge selectivity, and not a discrete binding site. However, charge-reversing mutations are potentially misleading because they introduce new charges that did not exist in the native protein and therefore may reflect artificially created electrostatic effects, rather than inform on the location of the normal selectivity filter.

Our findings also differ from those of Hou et al (2005). They performed charge-neutralizing mutations in claudin-16 and found five acidic residues in the first extracellular loop that affected cation permeability and were interspersed with other acidic residues that had no effect. Mutation of each of the five functionally important residues had only a modest effect (11–33% reduction in

P_{Na}), and combining the mutations appeared to be additive (Hou et al., 2005). At first sight, these results would seem to suggest that the first extracellular domain of claudin-16 is folded in such a way as to bring together the side groups of multiple acidic residues that are arranged nonlinearly, thus forming the selectivity filter. However, it is important to remember that replacement of a charged residue, even with a neutral residue, can have multiple consequences, including steric effects and disruption of folding due to the abolition of salt bridges, all of which could abrogate permeability. Thus, without specific studies to prove that the mutation directly affects electrostatic interaction between the pore and the permeating ion (such as alkali metal selectivity sequences and pH titration), the composition of the selectivity filter in claudin-16 remains unproven.

When the amino acid sequences of the first extracellular loop of all claudins are aligned (Fig. 12), one can observe that the homologous position to D65 in claudin-2 has a basic residue in the majority (15/22) of the other isoforms. The only other isoform with an acidic residue at this position is claudin-16, which also acts as a cation-selective pore. Furthermore, the next position downstream, 66, is also occupied by an acidic residue in claudin-16; the only other claudins that have an acidic residue here are 10b and 15, the only other known cation-selective, pore-forming claudins (Van Itallie et al., 2003, 2006), and 22 (whose function is unknown). Finally, position 64 is occupied by one of the two invariant cysteines found in the extracellular domain of all claudins, suggesting that it may have a structural role, perhaps in intramolecular disulfide bonding. We therefore postulate that C64 anchors the two residues at positions 65 and 66 so that their side chains protrude into the lumen of the pore and can contribute to an electrostatic cation interaction site.

Our Brownian dynamics simulations show that our experimental results can be mimicked by a very simple pore model. The tertiary structure of the extracellular domains of claudin has not yet been solved, and so several somewhat arbitrary assumptions had to be made to construct this first-pass model. Furthermore, we performed sensitivity analyses (see Online Supplemental Material II) to investigate the effect of the channel geometry, protein dielectric constants, and the effective charges and positions of D65 on ion permeation through the claudin-2 model pore. We found that over experimentally reasonable ranges of these parameters, the basic computational conclusions reached for the claudin-2 model pore developed herein did not change. The value of this model is that it clearly shows that two competing factors—the ion diffusivity and the ion size—can determine the relative permeability ratio of cations observed in the claudin-2. Additionally, it shows that the mere presence of D65 contributing the major intrapore charges could be sufficient to explain the observed cation selectivity. Interestingly, our method of modeling the intrapore charge and the permeating ions as fixed and mobile spheres, similar to the approach by Eisenman (1962), has yielded the first example of a Brownian dynamics model that can distinguish clearly between the permeabilities of the different alkali metal cations. In this model, consistent with experimental suggestion of dehydrated permeating cations, different alkali metal cations are assumed to be fully dehydrated (for simplification) and distinguished by their bare ion sizes and diffusivities. Ions having a smaller radius can approach the charge on D65 more closely, as well as giving it access to a larger accessible volume (entropic effects, i.e., excluded volume effect) in the selectivity filter. This increases the ion occupancy of the selectivity filter for smaller ions, and thus increases the permeability for smaller ions (see further discussion in the online supplemental material).

There are limitations to our model. Because of its simplicity it cannot simulate all aspects of claudin-2 behavior. Abolition of the charge on D65 does reduce P_{Na}. However, our computational model differs from our experimental findings in predicting that P_{Cl} would increase and that the alkali metal cation selectivity would not change appreciably (see online supplemental material). Further refinement of our first-pass model will be necessary to account for these observations, for example, by including more molecular detail in the modeling of the D65 residue (concerning both its geometric structure and the distribution of negative charge along this structure in the case of the anion form of the residue).

Not surprisingly, given that our model contains a discrete binding site, it predicts that the conductance–concentration relationship will be saturating at sufficiently high Na^+ concentrations. This is a testable prediction that would presumably distinguish it from a model in which multiple pore charges contribute to a diffuse electrostatic environment. So far our attempts to test this have been unsuccessful because supraphysiologic Na^+ concentrations have osmotic effects on the cell that disrupt transepithelial conductance (unpublished data).

Our model also predicts a single-pore conductance of 70 pS at the physiological Na^+ concentrations in which we observe a macroscopic claudin-2 conductance of $\sim$10 mS/cm^2. As discussed in the online supplemental material, the channel geometry and the choice of protein dielectric constant affect the predicted single-channel conductance. For example, while keeping all other parameters the same, a cylindrical channel with a uniform pore size of 3.25 and 32 Å in length gave a channel conductance almost 1.7 times smaller than the claudin-2 model with conical vestibules (same minimum pore size and channel length, but with a funnel-like channel entrance). However, despite some inevitable uncertainties regarding the claudin-2 model channel, our Brownian dynamics simulations together with the deduced

maximum channel conductance (with respect to variations in concentration as well as the assumed effective charge on D65) suggest a maximum single-channel conductance on the order of ~100 pS for claudin-2. MDCK cells are approximately hexagonal and have an average radius of 7 μm (Cereijido et al., 1983), and hence an area of 1.5×10^{-6} cm^2 and a cell perimeter of 42 μm. From this, we estimate that the conductance of the intercellular junction must be 100 pS per 100 nm. We do not explicitly account for strand number in our model, but assuming there are four identical strands in a series, we would estimate that there is one claudin-2 pore every 25 nm along each tight junction strand, a fairly low pore density.

In conclusion, our data suggest that claudin-2 forms narrow, water-filled cation-selective paracellular pores. Cation selectivity is achieved by a negatively charged site within the pore with which partially dehydrated permeating cations interact, and which can be titrated by pH. Our studies further suggest that a significant part of this interaction site is contributed by the carboxylate side chain of D65 and suggest that the homologous residues at positions 65 and 66 may play similar roles in other claudin family members. Thus, paracellular claudin-based pores use discrete intrapore electrostatic interactions to achieve high conductance together with charge selectivity.

We thank Drs. Alicia McDonough and Kwang Kim for sharing their equipment, and Dr. Robert Chow for reading an early version of the manuscript. We also wish to thank the reviewers, who played a collaborative role in revising aspects of this manuscript, particularly with regard to the method of correcting for liquid junction potentials. This turned out to be critical in arriving at quantitatively accurate data and changed our conclusions significantly, and has also led to a significant change in the way we now perform diffusion potential experiments in our laboratories.

This work was supported by National Institutes of Health grants DK062283 (to A.S.L. Yu), HL25822 (to E.E. Schneeberger), and DK48522 (to the USC Center for Liver Diseases, for the Confocal Microscopy Sub-Core). The work of M.H. Cheng and R.D. Coalson was supported in part by the National Science Foundation (grant CHE-0518044).

Lawrence G. Palmer served as editor.

Submitted: 3 November 2008
Accepted: 8 December 2008

REFERENCES

Alexandre, M.D., Q. Lu, and Y.H. Chen. 2005. Overexpression of claudin-7 decreases the paracellular Cl- conductance and increases the paracellular Na+ conductance in LLC-PK1 cells. *J. Cell Sci.* 118:2683–2693.

Amasheh, S., N. Meiri, A.H. Gitter, T. Schoneberg, J. Mankertz, J.D. Schulzke, and M. Fromm. 2002. Claudin-2 expression induces cation-selective channels in tight junctions of epithelial cells. *J. Cell Sci.* 115:4969–4976.

Andersen, O.S., and M. Fuchs. 1975. Potential energy barriers to ion transport within lipid bilayers. *Biophys. J.* 15:795–830.

Angelow, S., K.J. Kim, and A.S. Yu. 2006. Claudin-8 modulates paracellular permeability to acidic and basic ions in MDCK II cells. *J. Physiol.* 571:15–26.

Angelow, S., R. El-Husseini, S.A. Kanzawa, and A.S. Yu. 2007a. Renal localization and function of the tight junction protein, claudin-19. *Am. J. Physiol. Renal Physiol.* 293:F166–F177.

Angelow, S., E.E. Schneeberger, and A.S. Yu. 2007b. Claudin-8 expression in renal epithelial cells augments the paracellular barrier by replacing endogenous claudin-2. *J. Membr. Biol.* 215:147–159.

Barry, P.H., and J.M. Diamond. 1970. Junction potentials, electrode standard potentials, and other problems in interpreting electrical properties of membranes. *J. Membr. Biol.* 3:93–122.

Barry, P.H., J.M. Diamond, and E.M. Wright. 1971. The mechanism of cation permeation in the rabbit gallbladder: dilution potentials and biionic potentials. *J. Membr. Biol.* 4:358–394.

Cereijido, M., E.S. Robbins, W.J. Dolan, C.A. Rotunno, and D.D. Sabatini. 1978. Polarized monolayers formed by epithelial cells on a permeable and translucent support. *J. Cell Biol.* 77:853–880.

Cereijido, M., L. Gonzalez-Mariscal, and L. Borboa. 1983. Occluding junctions and paracellular pathways studied in monolayers of MDCK cells. *J. Exp. Biol.* 106:205–215.

Cheng, M.H., and R.D. Coalson. 2005. An accurate and efficient empirical approach for calculating the dielectric self energy and ion-ion pair potential in continuum models of biological ion channels. *J. Phys. Chem. B.* 109:488–498.

Cheng, M.H., M. Cascio, and R.D. Coalson. 2005. Theoretical studies of the M2 transmembrane segment of the glycine receptor: models of the open pore structure and current-voltage characteristics. *Biophys. J.* 89:1669–1680.

Cheng, M.H., A.B. Mamonov, J.W. Dukes, and R.D. Coalson. 2007. Modeling the fast gating mechanism in ClC-0 chloride channel. *J. Phys. Chem. B.* 111:5956–5965.

Colegio, O.R., C.M. Van Itallie, H.J. McCrea, C. Rahner, and J.M. Anderson. 2002. Claudins create charge-selective channels in the paracellular pathway between epithelial cells. *Am. J. Physiol. Cell Physiol.* 283:C142–C147.

Colegio, O.R., C. Van Itallie, C. Rahner, and J.M. Anderson. 2003. Claudin extracellular domains determine paracellular charge selectivity and resistance but not tight junction fibril architecture. *Am. J. Physiol. Cell Physiol.* 284:C1346–C1354.

Corry, B., T.W. Allen, S. Kuyucak, and S.H. Chung. 2001. Mechanisms of permeation and selectivity in calcium channels. *Biophys. J.* 80: 195–214.

Corry, B., T. Vora, and S.H. Chung. 2005. Electrostatic basis of valence selectivity in cationic channels. *Biochim. Biophys. Acta.* 1711: 72–86.

Diamond, J.M., and E.M. Wright. 1969. Biological membranes: the physical basis of ion and nonelectrolyte selectivity. *Annu. Rev. Physiol.* 31:581–646.

Dwyer, T.M., D.J. Adams, and B. Hille. 1980. The permeability of the endplate channel to organic cations in frog muscle. *J. Gen. Physiol.* 75:469–492.

Eisenman, G. 1962. Cation selective glass electrodes and their mode of operation. *Biophys. J.* 2:259–323.

Eisenman, G., and R. Horn. 1983. Ionic selectivity revisited: the role of kinetic and equilibrium processes in ion permeation through channels. *J. Membr. Biol.* 76:197–225.

Furuse, M., K. Furuse, H. Sasaki, and S. Tsukita. 2001. Conversion of zonulae occludentes from tight to leaky strand type by introducing claudin-2 into Madin-Darby canine kidney I cells. *J. Cell Biol.* 153: 263–272.

Gitter, A.H., M. Bertog, J. Schulzke, and M. Fromm. 1997. Measurement of paracellular epithelial conductivity by conductance scanning. *Pflugers Arch.* 434:830–840.

Graf, P., A. Nitzan, M.G. Kurnikova, and R.D. Coalson. 2000. A dynamic lattice Monte Carlo model of ion transport in inhomogeneous dielectric environments: method and implementations. *J. Phys. Chem. B.* 104:12324–12338.

Graf, P., M.G. Kurnikova, R.D. Coalson, and A. Nitzan. 2004. Comparison of dynamic lattice Monte-Carlo simulations and dielectric self energy Poisson-Nernst-Planck continuum theory for model ion channels. *J. Phys. Chem. B.* 108:2006–2015.

Green, W.N., and O.S. Andersen. 1991. Surface charges and ion channel function. *Annu. Rev. Physiol.* 53:341–359.

Hille, B. 2001. Ion Channels of Excitable Membranes. Sinauer, Sunderland, MA. 337 pp.

Hou, J., D.L. Paul, and D.A. Goodenough. 2005. Paracellin-1 and the modulation of ion selectivity of tight junctions. *J. Cell Sci.* 118: 5109–5118.

Hou, J., A. Renigunta, M. Konrad, A.S. Gomes, E.E. Schneeberger, D.L. Paul, S. Waldegger, and D.A. Goodenough. 2008. Claudin-16 and claudin-19 interact and form a cation-selective tight junction complex. *J. Clin. Invest.* 118:619–628.

Im, W., and B. Roux. 2002. Ions and counterions in a biological channel: a molecular dynamics simulation of OmpF porin from Escherichia coli in an explicit membrane with 1 M KCl aqueous salt solution. *J. Mol. Biol.* 319:1177–1197.

Imoto, K., C. Busch, B. Sakmann, M. Mishina, T. Konno, J. Nakai, H. Bujo, Y. Mori, K. Fukuda, and S. Numa. 1988. Rings of negatively charged amino acids determine the acetylcholine receptor channel conductance. *Nature.* 335:645–648.

Kimizuka, H., and K. Koketsu. 1964. Ion transport through cell membrane. *J. Theor. Biol.* 6:290–305.

Mamonov, A.B., M.G. Kurnikova, and R.D. Coalson. 2006. Diffusion constant of K+ inside Gramicidin A: a comparative study of four computational methods. *Biophys. Chem.* 124:268–278.

Mitic, L.L., V.M. Unger, and J.M. Anderson. 2003. Expression, solubilization, and biochemical characterization of the tight junction transmembrane protein claudin-4. *Protein Sci.* 12:218–227.

Nightingale, E.R. 1959. Phenomenological theory of ion solvation. Effective radii of hydrated ions. *J. Phys. Chem.* 63:1381–1387.

O'Mara, M., P.H. Barry, and S.H. Chung. 2003. A model of the glycine receptor deduced from Brownian dynamics studies. *Proc. Natl. Acad. Sci. USA.* 100:4310–4315.

Pauling, L. 1948. The Nature of the Chemical Bond. Cornell University Press, Ithaca, NY. 450 pp.

Pethig, R. 1979. Dielectric and Electronic Properties of Biological Materials. Wiley, Chichester, UK. 376 pp.

Pitera, J.W., M. Falta, and W.F. van Gunsteren. 2001. Dielectric properties of proteins from simulation: the effects of solvent, ligands, pH, and temperature. *Biophys. J.* 80:2546–2555.

Renkin, E.M. 1954. Filtration, diffusion and molecular sieving through porous cellulose membranes. *J. Gen. Physiol.* 38:225–243.

Reuss, L. 2001. Tight junction permeability to ions and water. *In* Tight Junctions. M. Cereijido and J. Anderson, editors. CRC Press, Boca Raton, FL. 61–88.

Simonson, T., and I.C.L. Brooks. 1996. Charge screening and the dielectric constant of proteins: insights from molecular dynamics. *J. Am. Chem. Soc.* 118:8452–8458.

Smith, P.E., R.M. Brunne, A.E. Mark, and W.F. Van Gunsteren. 1993. Dielectric properties of trypsin inhibitor and lysozyme calculated from molecular dynamics simulations. *J. Phys. Chem.* 97: 2009–2014.

Tsukita, S., and M. Furuse. 2000. Pores in the wall: claudins constitute tight junction strands containing aqueous pores. *J. Cell Biol.* 149:13–16.

Van Itallie, C., C. Rahner, and J.M. Anderson. 2001. Regulated expression of claudin-4 decreases paracellular conductance through a selective decrease in sodium permeability. *J. Clin. Invest.* 107: 1319–1327.

Van Itallie, C., A.S. Fanning, and J.M. Anderson. 2003. Reversal of charge selectivity in cation or anion selective epithelial lines by expression of different claudins. *Am. J. Physiol. Cell Physiol.* 286:F1078–F1084.

Van Itallie, C.M., and J.M. Anderson. 2006. Claudins and epithelial paracellular transport. *Annu. Rev. Physiol.* 68:403–429.

Van Itallie, C.M., S. Rogan, A.S. Yu, L. Seminario-Vidal, J. Holmes, and J.M. Anderson. 2006. Two splice variants of claudin-10 in the kidney create paracellular pores with different ion selectivities. *Am. J. Physiol. Renal Physiol.* 291:F1288–F1299.

Van Itallie, C.M., J. Holmes, A. Bridges, J.L. Gookin, M.R. Coccaro, W. Proctor, O.R. Colegio, and J.M. Anderson. 2008. The density of small tight junction pores varies among cell types and is increased by expression of claudin-2. *J. Cell Sci.* 121:298–305.

Wright, E.M., P.H. Barry, and J.M. Diamond. 1971. The mechanism of cation permeation in the rabbit gallbladder: conductances, the current-voltage relation, the concentration dependence of anion-cation discrimination, and the calcium competition effect. *J. Membr. Biol.* 4:331–357.

Yu, A.S., A.H. Enck, W.I. Lencer, and E.E. Schneeberger. 2003. Claudin-8 expression in MDCK cells augments the paracellular barrier to cation permeation. *J. Biol. Chem.* 278:17350–17359.